communications physics

ARTICLE

https://doi.org/10.1038/s42005-022-00898-z OPEN

Order to disorder in quasiperiodic composites

David Morison[1], N. Benjamin Murphy[2], Elena Cherkaev[2] & Kenneth M. Golden[2]✉

From quasicrystalline alloys to twisted bilayer graphene, the study of material properties arising from quasiperiodic structure has driven advances in theory and applied science. Here we introduce a class of two-phase composites, structured by deterministic Moiré patterns, and we find that these composites display exotic behavior in their bulk electrical, magnetic, diffusive, thermal, and optical properties. With a slight change in the twist angle, the microstructure goes from periodic to quasiperiodic, and the transport properties switch from those of ordered to randomly disordered materials. This transition is apparent when we distill the relationship between classical transport coefficients and microgeometry into the spectral properties of an operator analogous to the Hamiltonian in quantum physics. We observe this order to disorder transition in terms of band gaps, field localization, and mobility edges analogous to Anderson transitions — even though there are no wave scattering or interference effects at play here.

[1] Department of Physics & Astronomy, University of Utah, 115 S 1400 E, Salt Lake City, UT 84112-0830, USA. [2] Department of Mathematics, University of Utah, 155 S 1400 E, Salt Lake City, UT 84112-0090, USA. ✉email: golden@math.utah.edu

In the late 1980s it was shown that in a composite patterned after a crystal, such as a dielectric material with a periodic lattice of voids, electromagnetic waves of certain frequencies and directions could be prohibited from propagating within the structure[1,2]. This observation established a powerful analogy relating photonic band gaps to electronic band gaps in metals and other condensed matter. Thus solid state physics and Anderson localization was brought to optics[1–4], leading to the development of photonic crystals and theories of controlling the flow of light through structured media. The discovery of quasicrystals[5–7] demonstrated that geometries with predictable long range order but no periodicity could play an important role in physics and materials science. This led to the development of photonic quasicrystals[8–17], with the conceptual framework again provided by the analogy with quantum transport in solid-state physics.

Motivated by these findings and the highly active field of twisted graphene bilayers[18], with Moiré patterns tuned by the twist angle to take periodic and aperiodic geometries, here we construct a class of deterministic, two-phase Moiré-structured composite materials in two dimensions. This construction enables us to study in several physical settings how classical transport behaves in the transition from periodicity to aperiodicity. Indeed, rather than a governing wave equation like Schrödinger's equation for quantum transport or the classical wave equation for electromagnetic transport[17,19–21], problems involving electrical conductivity σ, thermal conductivity κ, complex permittivity ϵ in the quasistatic limit, or diffusivity D can all be formulated in terms of the same divergence form second-order elliptic equation (2) below, and do not involve any wave interference or scattering effects. Bulk behavior is analyzed in terms of the Bergman-Milton (or Stieltjes integral) representation, which holds for the effective parameters σ^*, κ^*, ϵ^*, D^*, etc.[22–25]. It involves a spectral measure μ of a self-adjoint operator G, which plays the role of the quantum physics Hamiltonian and depends only on the mixture geometry. In discrete settings, G is a real-symmetric matrix. The measure μ, local electric field $\mathbf{E}$, displacement $\mathbf{D} = \epsilon\mathbf{E}$ and current $\mathbf{J} = \sigma\mathbf{E}$ are all determined by the eigenvalues and eigenvectors of G. One of our main results is that through this spectral distillation and recent results on computing μ[26] and analyzing its behavior with random matrix theory[27], we establish a powerful analogy between various classical transport processes in periodic and quasiperiodic composites, and quantum transport with localization and band gaps in solid state physics, as was done for optics in photonic crystals and quasicrystals in the scattering regime. We emphasize, however, that our results apply broadly to transport phenomena in settings described by Eq. (2), with no restriction on the length scales in the systems involved, except for the condition imposed on the microstructural scale by the quasistatic assumption that must be satisfied in the context of complex permittivity.

Results and discussion

We find that as the geometry is tuned from periodic to quasiperiodic, the eigenvalues, eigenmodes, profile of ϵ^*, and localization properties of $\mathbf{E}$ undergo an order-to-disorder transition analogous to the Anderson transition. Our results are described in the (quasistatic) electromagnetic case, but we keep in mind their broad applicability. Spectral measures for periodic systems have sharp resonances that induce dramatic variability in band and absorption characteristics, and in profiles of ϵ^*. Regions of extended eigenstates are separated by "mobility edges" of localized states, and $\mathbf{E}$ is localized for certain frequencies and extended for others. As the geometry is tuned to aperiodicity, the behavior of μ and ϵ^* resembles that of the 2D random percolation model at its threshold, with a regularly distributed mixture of localized and extended eigenstates giving rise to tenuously connected current paths, pronounced spectral endpoint behavior, and Wigner-Dyson eigenvalue statistics with strong level repulsion[27].

Our investigation here of quasiperiodic media was motivated not only by the findings for random media in ref. [27], but by much earlier studies which revealed sensitive, discontinuous dependence of bulk transport on the variations in local properties[28,29]. For example, it was found in one dimension with local conductivity $\sigma(x) = 3 + \cos x + \cos kx$, which is periodic for k rational and quasiperiodic for k irrational, that the effective conductivity $\sigma^*(k)$ is discontinuous in k[28], with 2D examples in ref. [29]. These studies, in turn, were motivated by the discovery of quasicrystals and findings on the spectrum of Hamiltonians with quasiperiodic potentials[30–32].

The spectral characteristics considered here govern the optical properties of nanostructured bimetallic films[33,34] and depositions of nanosized metal particles on thin dielectric substrates[35–38], which change as a function of heterogeneous surface structure composition and geometry. This enables tunability of their optical responses for nano-plasmonic device applications[33–38]. The long wavelength quasistatic assumption holds in the visible range[39], and these systems are described macroscopically by the Stieltjes integral representations for ϵ^* or σ^*. Resonances in μ explain giant surface-enhanced Raman scattering observed in semicontinuous films[34,40,41], and induce strong fluctuations in $\mathbf{E}$ and the dielectric profile of ϵ^*, associated with the excitation of collective electronic surface plasmon modes[39]. We numerically explore these phenomena in 2D impedance networks with quasiperiodic microgeometry and discuss our results using Anderson transition interpretations of random matrix theory.

Effective transport in composites with Moiré-structured microgeometry

We begin by introducing a class of 2D two-component composites whose microgeometries are based on Moiré patterns, and are tunable to be periodic or aperiodic.

Constructing Moiré patterns. Consider the square bond lattice joining nearest neighbor points in $\mathbb{Z}^2$, with standard basis vectors $\mathbf{e}_1$ and $\mathbf{e}_2$, and the scaled rotation transformation T defined for $(x, y) \in \mathbb{R}^2$ by

$$T : (x, y) \mapsto (a, b), \qquad T = r\begin{pmatrix} \cos\theta & -\sin\theta \\ \sin\theta & \cos\theta \end{pmatrix}. \tag{1}$$

The mixture geometry of the two phases is determined by the characteristic function χ_1, taking the value $\chi_1 = 1$ in material phase 1 and zero otherwise, with $\chi_2 = 1 - \chi_1$. The system microgeometry is constructed from the periodic function $\psi(a, b) = \cos(2\pi a)\cos(2\pi b)$ and the condition $\chi_1(x, y) = 1$ for all $(x, y) \in \mathbb{R}^2$ such that $\psi(T(x, y)) \geq \psi_0$, and is zero otherwise. We focus on the value $\psi_0 = 0$, which generates in the underlying bond lattice a discretized composite microstructure with a fraction $p \approx 1/2$ of type one bonds. We do so to compare features of deterministically tuned quasiperiodic systems to those of the random percolation model near the percolation transition $p = p_c = 1/2$[42,43].

Primitive translation vectors for ψ are $\mathbf{t}_1 = (1/2, 1/2)$ and $\mathbf{t}_2 = (1/2, -1/2)$. When r and θ are chosen such that $T : (m\mathbf{e}_1 + n\mathbf{e}_2) \mapsto (m'\mathbf{t}_1 + n'\mathbf{t}_2)$ for integer values of m, n, m' and n', then χ_1 has a finite period of, at most, $K = \sqrt{m^2 + n^2}$, and has infinite

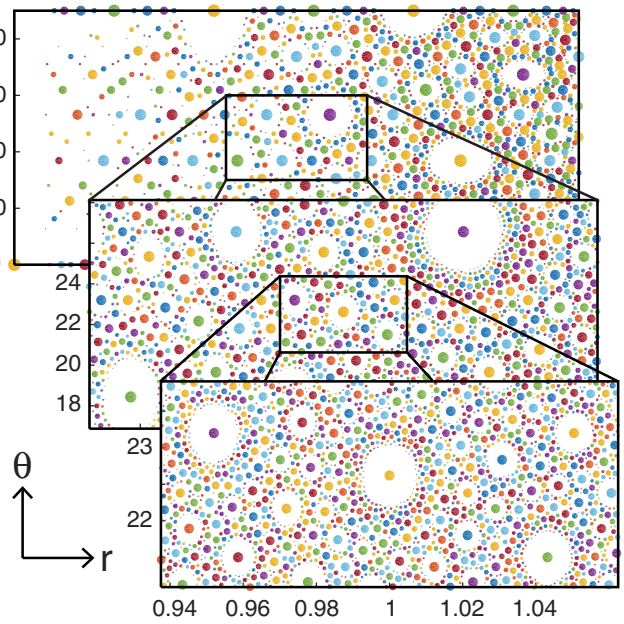

Fig. 1 Fractal arrangement of periodic systems. Sequential insets zooming into smaller regions of parameter space. Dots identify Moiré parameter (r, θ) values corresponding to systems with periodic microgeometry, where short and large periods are identified by large and small dots, respectively, revealing self similar, fractal arrangements of periodic systems.

period otherwise. The arrangement of r and θ such that $K < \infty$ is fractal in nature, as shown in Fig. 1. The arrangement of (r, θ) values associated with finite periods is similar to fractal distributions defined in terms of rational numbers on the real line, such as Thomae's function[29].

An integral representation for effective transport coefficients. The effective behavior of macroscopic transport in two-phase composite materials is described by homogenized coefficients including electrical and thermal conductivity, diffusivity, complex permittivity, and magnetic permeability. These can all be defined in terms of the same elliptic partial differential equation[25,43]. For complex permittivity in the quasistatic regime, such as the metal-dielectric mixtures in visible light discussed above, the system is described locally by

$$\nabla \cdot (\epsilon \nabla \phi) = 0, \tag{2}$$

with potential ϕ, electric field $\mathbf{E} = -\nabla\phi$, displacement $\mathbf{D} = \epsilon\mathbf{E}$, and local complex permittivity $\epsilon(x, y)$ taking frequency-dependent values $\epsilon_1(\omega)$ or $\epsilon_2(\omega)$, where $\langle \mathbf{E} \rangle = \mathbf{E}_0$ and $\langle \cdot \rangle$ denotes spatial average. The fields $\mathbf{E}$ and $\mathbf{D}$ satisfy $\nabla \times \mathbf{E} = 0$ and $\nabla \cdot \mathbf{D} = 0$, with $\epsilon = \epsilon_1\chi_1 + \epsilon_2\chi_2$. See refs. [24–26] for a "weak" formulation of this problem that rigorously accounts for the discontinuous, and thus non-differentiable nature of the parameter $\epsilon(x, y)$ in Eq. (2).

The effective permittivity matrix $\boldsymbol{\epsilon}^*$ can be defined by $\langle \mathbf{D} \rangle = \boldsymbol{\epsilon}^* \langle \mathbf{E} \rangle$ with $\langle \mathbf{E} \rangle = \mathbf{E}_0$, where $\mathbf{E}_0 = E_0\,\mathbf{e}_k$ for some standard basis vector $\mathbf{e}_k$, $k = 1, \ldots, d$, where d is dimension. Equivalently, it can be defined in terms of system energy using $\langle \mathbf{D} \cdot \mathbf{E} \rangle = \epsilon^*_{kk} E_0^2$, where ϵ^*_{kk} is the kth diagonal coefficient of the matrix $\boldsymbol{\epsilon}^*$, which we denote by $\epsilon^* = \epsilon^*_{kk}$. Thus, the effective parameter characterizes a homogeneous medium immersed in a uniform field $\mathbf{E}_0$ that behaves macroscopically and energetically as does the inhomogeneous composite medium.

The key step in the analytic continuation method[22–26] is the Stieltjes integral representation for ϵ^*,

$$F(s) = 1 - \frac{\epsilon^*}{\epsilon_2} = \int_0^1 \frac{d\mu(\lambda)}{s - \lambda}, \quad s = \frac{1}{1 - \epsilon_1/\epsilon_2}. \tag{3}$$

Here, $F(s) = \langle \chi_1 \mathbf{E} \cdot \mathbf{E}_0 \rangle / (sE_0^2)$ and $-F(s)$ plays the role of an effective electric susceptibility. Equation (3) follows from applying the operator $-\nabla(-\Delta)^{-1}$ to Eq. (2) and writing it as $\Gamma\mathbf{D} = 0$, where $\Gamma = -\nabla(-\Delta)^{-1}\nabla\cdot$ is an orthogonal projection onto curl-free fields and is based on convolution with the Green's function for the Laplacian $\Delta = \nabla^2$ [24,26]. Then using $\epsilon = \epsilon_1\chi_1 + \epsilon_2\chi_2 = \epsilon_2(1 - \chi_1/s)$ and $\Gamma\nabla\phi = \nabla\phi$ yields the resolvent representation

$$\chi_1 \mathbf{E} = s(sI - G)^{-1}\chi_1 \mathbf{E}_0, \quad G = \chi_1 \Gamma \chi_1, \tag{4}$$

involving the self-adjoint operator $G = \chi_1\Gamma\chi_1$ [24,26]. Applying the spectral theorem to $F(s) = \langle \chi_1 \mathbf{E} \cdot \mathbf{E}_0 \rangle / (sE_0^2)$ then yields[24,26] equation (3), where μ is a spectral measure of the operator G.

A key feature of Eqs. (3) and (4) is that the material parameters in s and the applied field strength E_0 are separated from the geometric complexity of the system, which is encoded in the properties of the spectral measure μ and its moments $\mu_n = \int_0^1 \lambda^n\, d\mu(\lambda)$. For example, $\mu_0 = \langle \chi_1 \rangle = p$, the volume fraction (or area fraction) of medium 1. All of the effective coefficients of the composite material mentioned above are represented by Stieltjes integrals with the same μ[44].

While the measure μ can include discrete and/or continuous components[25], it reduces to a weighted sum of Dirac δ-functions $\delta(\lambda - \lambda_j)$ for media such as laminates, hierarchical coated cylinder and sphere assemblages, and finite *RLC* impedance networks[22–26]. Here, we investigate effective transport properties of square two-component impedance networks in 2D of size M with periodic and quasiperiodic microgeometry. In this setting, $G = \chi_1\Gamma\chi_1$ is a real-symmetric matrix of size $N = 2M^2$, χ_1 is a diagonal matrix with 1's and 0's along the diagonal corresponding to impedance type, and $\Gamma = \nabla(\nabla^T\nabla)^{-1}\nabla^T$ is a projection matrix, where ∇ is a finite difference matrix representation of the differential operator ∇ [26]. The measure μ is determined by the eigenvalues λ_j and eigenvectors $\mathbf{v}_j$ of $N_1 \times N_1$ submatrices of Γ with rows and columns corresponding to the diagonal components $[\chi_1]_{jj} = 1$, with

$$d\mu(\lambda) = \sum_j m_j\, \delta(\lambda - \lambda_j)\, d\lambda, \quad m_j = \left(\mathbf{v}_j \cdot \chi_1 \hat{\mathbf{e}}_k\right)^2, \tag{5}$$

$j = 1, \ldots, N_1$, $N_1 \approx pN$ (total number of ϵ_1 bonds), and $\hat{\mathbf{e}}_k$ is a standard basis vector in $\mathbb{R}^{N_1}$ [26,27]. In this case, Eqs. (3) and (4) become finite sums with

$$F(s) = 1 - \frac{\epsilon^*}{\epsilon_2} = \sum_j \frac{m_j}{s - \lambda_j}, \qquad \chi_1 \mathbf{E} = sE_0 \sum_j \frac{(\mathbf{v}_j \cdot \chi_1 \hat{\mathbf{e}}_k)}{s - \lambda_j}\, \mathbf{v}_j, \tag{6}$$

given explicitly in terms of the λ_j and eigenvectors $\mathbf{v}_j$ of G[26].

In the next section, we compute the spectral measure μ, hence the local fields and the effective complex permittivity ϵ^* for the Moiré-structured class of composite materials described by Eq. (1) above. We interpret the frequency dependent behavior of physical quantities such as the phase and amplitude of ϵ^*, and localization and intensity of $\mathbf{E}$ and $\mathbf{D}$, in terms of spectral properties of μ and Anderson transition interpretations of random matrix theory.

Analysis

The Moiré system introduced above is parameterized by $r > 0$ and $0 \le \theta < 2\pi$, which generates a diverse assortment of periodic ("finite period") and quasiperiodic ("infinte period") microgeometries. To numerically calculate mathematical and physical

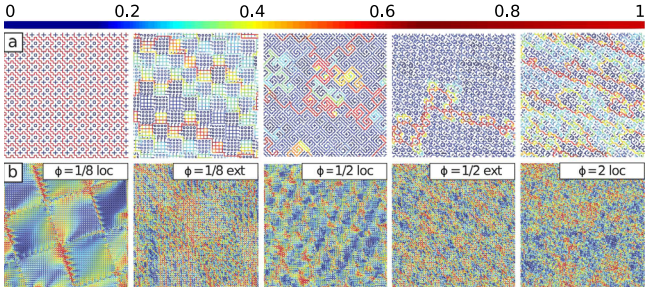

Fig. 2 Quasiperiodic composite microgeometry and Anderson localization of fields. Moiré interference patterns generated by the transformation Eq. (1) give rise to a large class of composite materials with periodic and quasiperiodic microgeometry. (**a**) Various example subsections arising from different Moiré parameter pairs (r, θ). Microgeometries in (**a**) are shown with square system sizes 53 for the far left and 73 for all others, small enough to resolve the small-scale detail yet illustrate the large geometric variety. Geometry is illustrated by rendering $\chi_1 = 1$ bonds and omitting $\chi_1 = 0$ bonds. Cool and warm colors correspond to near-zero and large values of electric field $|\chi_1\mathbf{E}|$ or displacement $|\chi_1\mathbf{D}|$, respectively, with the color bar at the top showing the saturated linear scale, normalized to the unit interval. (**b**) Anderson localization of fields in quasiperiodic media. Departure from short period system geometry is parameterized by ϕ. Composite microgeometry parameterized by $r = \sqrt{10}/3$ and $\theta = \arctan(1/3) + \phi$ for $0° \le \phi \le 2°$ with system size 199. For small values of ϕ, the fields exhibit a frequency dependent transition from localized (loc) to extended (ext). Identical values of ϕ correspond to identical microgeometries, and the differences in the values of $|\chi_1\mathbf{E}|$ are solely due to frequency ω dependent material properties for different values of ω. As $\phi \to 2$, the local fields become similar for all frequencies away from $\omega = 0$, qualitatively resembling the rightmost panel in (**b**) (as well as that of the percolation model near the percolation threshold $p = p_c$[27]). The inverse participation ratio (IPR) providess quantitative description of this localization phenomenon.

quantities, we consider finite subsets of these systems as *RLC* impedance networks. Different types of microgeometries in this class are displayed in Fig. 2a with small enough system sizes to resolve the small-scale geometry while still illustrating the large variety in structure, hinting at the geometric richness of our Moiré composites. The bond color indicates the modulus value of **E**, i.e., $|\chi_1\mathbf{E}|$, calculated via Eq. (6). Since $\chi_1\mathbf{D} = \epsilon_1\chi_1\mathbf{E}$ these colors also specify displacement values with a change in scale by $|\epsilon_1|$. We therefore normalize the computed fields to take values in the unit interval.

It was shown in ref. [26] that expressions known in closed form for the 2D percolation model in the infinite volume limit are well approximated by ensemble averages of systems of size ≈70 and by single systems of size ≈200. The Moiré-structured composites studied here can have coherent structures on large length scales. However, we found for a system size of 199 that fluctuations present for smaller systems have essentially stabilized, with numerical results visually identical for larger system sizes, e.g., ≈250. A systematic study of system size dependence of quantities and finite size effects is interesting and useful but beyond the scope of the current manuscript.

Transport behavior in microstructures along a short trajectory in parameter space. In this section, we investigate a small swath of the large parameter space, for $r = \sqrt{10}/3$ and $\theta = \arctan(1/3) + \phi$ for $0° \le \phi \le 2°$, starting from a short period system. Figures 2b and 3a display examples of this region of parameter space and show that such a small change in the Moiré twist angle θ gives rise to a dramatic transition in composite microgeometry — from a short period system with orderly field (or current) paths to quasiperiodic systems with disorderly, meandering paths similar to those exhibited by the random percolation model near $p = p_c$.

When the fields are plotted versus $s(\omega)$, $0 \le \mathrm{Re}\, s(\omega) \le 1$ with $\mathrm{Im}\, s(\omega) \ll 1$ a frequency dependent localization/delocalization transition of fields is revealed for small values of $\phi \in [0, 2]$, as shown in Figure 2b for $\phi = 1/8$ and 1/2. In contrast, the fields for angles closer to $\phi = 2$ are more disordered and resemble those in the random percolation model, and are qualitatively similar to the rightmost panel in Figure 2b for all $0 < \mathrm{Re}\, s \le 1$. We investigate these and other phenomena through mathematical and physical quantities such as the spectral measure μ, correlations of its eigenvalues, localization of its eigenvectors, phase and magnitude of ϵ^*, localization and intensity of **E**, etc.

A large variety of physical phenomena exhibited by inhomogeneous materials can be described by two-component *RLC* impedance networks[40]. Each of the two components is created by combining a resistor R, inductor L, and capacitor C in a way that achieves an impedance characteristic of the material being modeled. For example, a Drude-metal/dielectric composite is modeled by R and L in series, in parallel with C for one component, and C for the other[39], yielding a plasma frequency $\omega_p^2 = 1/LC$ and relaxation time $\tau = L/R$. As Kirchhoff's network laws are discrete versions of the curl-free and divergence-free conditions on the fields in Eq. (1), these *RLC* impedance networks really do resemble the continuum composites they are intended to model[39].

Indeed, the AC response and polarization effects observed in a variety of conductor-dielectric mixtures at low frequencies are modeled by an $R - C$ network, while metal-dielectric composites exhibiting collective electronic modes at higher, optical frequencies such as (surface) plasmon resonances are modeled by an $RL - C$ network[40,41]. The dependence of $s(\omega)$ on frequency ω is model specific. For the $R - C$ and $RL - C$ models, $0 \le \mathrm{Re}\, s < 1$ for $0 \le \omega < \infty$ and $\delta \le \mathrm{Im}\, s < 0$, where $|\delta|$ can be chosen as small as desired, with $\mathrm{Re}\, s \to 1$ and $\mathrm{Im}\, s \to 0$ as ω increases[40,41]. In order to give a model independent description of the phenomena investigated here, we plot s-dependent quantities using $0 \le \mathrm{Re}\, s \le 1$ and $\mathrm{Im}\, s = 0.001$ fixed. For the sake of discussion, we describe our results in terms of the optical regime for the Drude model for gold/vacuum composites, which roughly corresponds to the interval $\mathrm{Re}\ s \lessapprox 0.2$. The optical regime for other material combinations corresponds to values of $\mathrm{Re}\, s$ throughout the unit interval[45].

As the frequency changes and $s(\omega)$ sweeps across the complex plane, with $s(0) = 0$, the spectral measure μ, distribution of its eigenvalues, and localization properties of its eigenvectors, shown in Fig. 3, govern the frequency dependence of the phase and magnitude of ϵ^* and the intensity and localization of **E** and **D**, shown in Fig. 4, according to the formulas in Eq. (6). Keeping these formulas with $\mathrm{Im}\, s(\omega) \ll 1$ in mind, we call resonant frequencies the values of ω where $\mathrm{Re}\, s(\omega) \approx \lambda_j$ and the masses m_j of μ are largest (shown in red in Fig. 3) and/or there's a large density of eigenvalues λ_j with moderate to large values of m_j.

For the short period system with $\phi = 0$ shown in Figure 3a, the spectral measure μ in Figure 3b is comprised of sharply peaked resonances. As ϕ increases and the composite microgeometry becomes quasiperiodic, the resonant frequencies away from $\omega = 0$ ($\lambda = 0$) spread out, change frequency locations, and diminish in strength. As $\phi \to 2$, the resonances in μ continue to spread out until all but the Drude resonance at $\omega = 0$ diminish, and μ and ϵ^* begin to resemble those of the random percolation model for $p = p_c$, shown in the rightmost panels of Fig. 3.

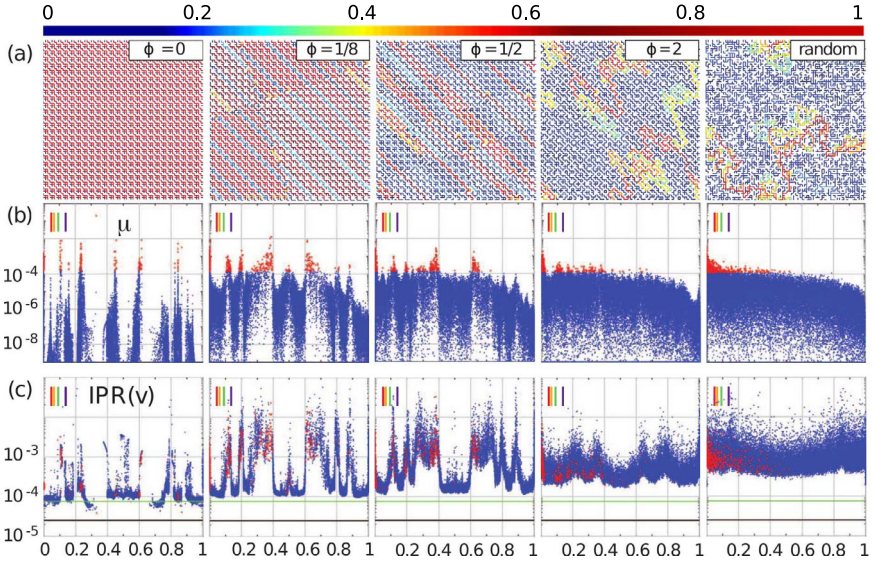

Fig. 3 Frequency profile of the spectral measure and eigenvector localization. Composite microgeometry and fields, spectral measure μ, and eigenvector inverse participation ration (IPR) plotted for various values of the Moiré twist angle θ, for $0° \le \phi \le 2°$, scale parameter $r = \sqrt{10}/3$, and square system of size 73 in (**a**) to show detail and of size 199 in (**b**) and (**c**). The color bars in the upper left of the panels are for reference and indicate Re $s(\omega)$ corresponding to impedances throughout the optical frequency range for a Drude model of a gold/vacuum composite. (**a**) Composite microgeometry and field intensity. Cool and warm colors correspond to near-zero and large values of electric filed $|\chi_1\mathbf{E}|$ or displacement $|\chi_1\mathbf{D}|$, respectively, with color bar at the top showing the saturated linear scale. (**b**) Masses m_j of measure μ plotted versus eigenvalues $0 \le \lambda_j \le 1$ of the matrix G. Red dots indicate the largest masses, used as indicators in (**c**) below. (**c**) IPR values for the eigenvectors $\mathbf{v}_j$ of G, IPR($\mathbf{v}$), plotted versus λ_j. Green and black horizontal lines indicate IPR values for Gaussian orthogonal ensemble (GOE) vectors and completely extended vectors, $3/N_1$ and $1/N_1$, respectively. These quantities for the random percolation model at the percolation transition, $p = p_c = 1/2$, are shown in the rightmost panels for comparison.

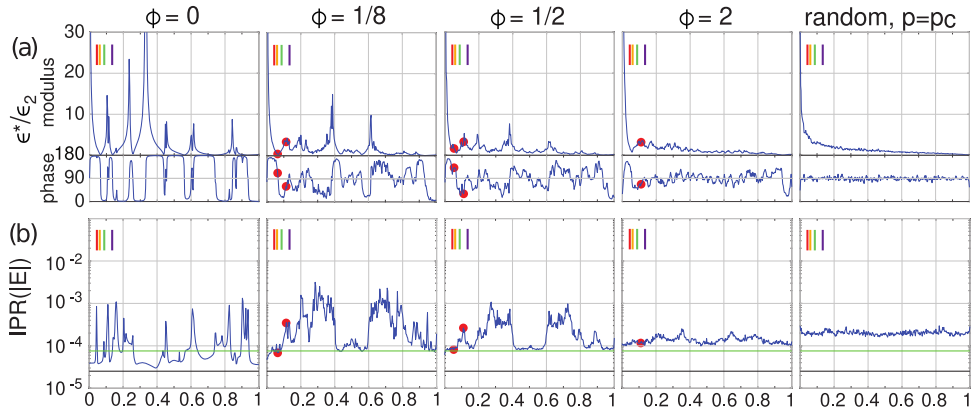

Fig. 4 Frequency dependence of dielectric profile and field localization. Relative effective complex permittivity ϵ^*/ϵ_2 and inverse participation ratio (IPR) of the modulus of the electric field, $|\chi_1\mathbf{E}|$, normalized to unity, IPR($\mathbf{E}$), plotted versus $0 \le \mathrm{Re}\, s \le 1$ for $\mathrm{Im}\, s = 0.001$ and various values of the Moiré twist angle θ and $r = \sqrt{10}/3$, for change in twist angle $0° \le \phi \le 2°$. The color bars in the upper left of the panels are for reference and indicate Re $s(\omega)$ for the optical frequency range for impedances corresponding to the Drude model for a gold/vacuum composite. (**a**) Amplitude and phase of ϵ^*/ϵ_2. (**b**) IPR($\mathbf{E}$) or equivalently IPR($\mathbf{D}$). These quantities for the random percolation model at the percolation transition, $p = p_c = 1/2$, are shown in the rightmost panels for comparison. The red dots in (**a**) and (**b**) identify values of dependant variable Re s used in Fig. 2b: for $\phi = 1/8$, Re $s = 0.063, 0.115$, for $\phi = 1/2$, Re $s = 0.055, 0.111$, and for $\phi = 2$, Re $s = 0.111$.

Resonances in μ have a physical interpretation in terms of relaxation times in the transient response in the $R-C$ model, or in terms of dielectric resonances in the $RL-C$ model[40,41]. The dielectric resonances observed for the $RL-C$ model with percolative geometry have been argued to provide a natural explanation for the anomalous fluctuations of the local electric field $\mathbf{E}$, which are responsible for giant surface-enhanced Raman scattering observed, for example, in semicontinuous metal films[41]. We show that the resonances in μ shown in Fig. 3 give rise to dramatic fluctuations in the amplitude and phase of ϵ^* and the intensity of the fields $\mathbf{E}$ and $\mathbf{D}$.

The inverse participation ratio (IPR) characterizes vector localization phenomenon. For an N_1-dimensional unit vector $\mathbf{u}$ it is given by $\mathrm{IPR}(\mathbf{u}) = \sum_i u_i^4$, where u_i is the ith component of the vector $\mathbf{u}$, $i = 1, \ldots, N_1$, and satisfies $\mathrm{IPR}(\mathbf{u}) = 1$ for a completely localized vector with only one non-zero component and $\mathrm{IPR}(\mathbf{u}) = 1/N_1$ for a completely extended vector with all components equal in value[27]. For matrices in the Gaussian orthogonal ensemble (GOE), the eigenvectors are quite extended with a mean asymptotic IPR value of $\mathrm{IPR}_{\mathrm{GOE}} = 3/N_1$[27].

Figure 3c displays IPR($\mathbf{v}_j$) for the eigenvectors $\mathbf{v}_j$, $j = 1, \ldots, N_1$, of G for various values of ϕ, as a function of the eigenvalues λ_j. The red dots in Fig. 3b, c for $\phi = 0$ and 1/8 show that resonant frequencies correspond either to very extended eigenvectors or "mobility edges" where the values IPR($\mathbf{v}_j$) have large variability

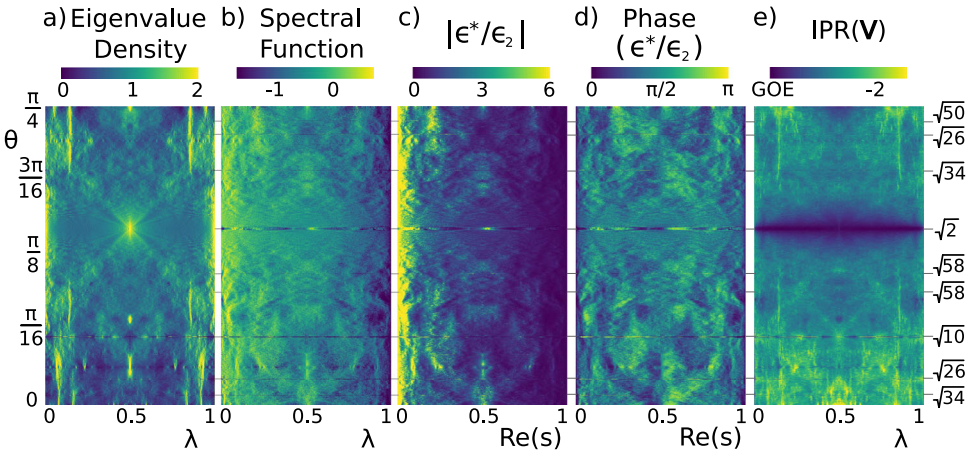

Fig. 5 Twist angle dependence. (**a**) Eigenvalue density $\rho(\lambda,\theta)$ (a histogram representation of the density of states $\sum_j \delta(\lambda-\lambda_j)/N_1$), (**b**) the spectral function $\mu(\lambda,\theta)$ (a kernel estimate representation of the spectral measure), (**c**) magnitude and (**d**) phase of relative effective complex permittivity ϵ^*/ϵ_2, and (**e**) a histogram-like representation of the inverse participation ratio (IPR) (median IPR of eigenstates associated with each bin – to distinguish mobility edges), all plotted versus the Moiré twist angle θ for scale parameter $r=\sqrt{5}/2$. We plot these quantities for one full period $0\le\theta\le\pi/4$. (**a**), (**b**), and (**e**) are plotted versus eigenvalue $0\le\lambda\le1$, while (**c**) and (**d**) are plotted versus $0\le Re\, s\le1$ for $\mathrm{Im}\, s=0.001$. Low and high density for ρ and μ and are indicated by dark blue and yellow, respectively, as shown by the color bars (with linear scale in (**a**), (**c**), and (**e**) and log_{10} scale in (**b**) and (**e**), slightly saturated at the ends to reveal more detail). Short period systems appear as horizontal streaks; for ρ and μ sharp isolated resonances are identified by localized yellow resonant peaks surrounded by dark blue troughs with values orders of magnitude smaller. The influence of μ on ϵ^*/ϵ_2 is clear, with striking similarities. For the IPR in (**e**) extended and localized vectors are identified by dark blue (with GOE value labeled) and yellow, with mobility edges indicated by sudden changes from one extreme to the other. Some of the θ values associated with these short period systems are identified by black tick marks on the right, labeled by the bound $K=\sqrt{m^2+n^2}$ on the system period.

for small changes in λ_j. As ϕ increases and the microgeometry becomes quasiperiodic, the mobility edges diminish as the values IPR($\mathbf{v}_j$) become more regularly distributed and qualitatively similar for all $0<\mathrm{Re}\, s(\omega)\le1$ away from the Drude peak at $\omega=0$, as shown in the two rightmost panels of Fig. 3b. As $\phi\to2$, the IPR($\mathbf{v}_j$) resemble those of the random percolation model at its threshold $p=p_c=1/2$, as shown in the rightmost panel of Fig. 3c.

The frequencies corresponding to resonances of μ and field delocalization are tunable through the quasiperiodic microgeometry via the scale parameter r and Moiré twist angle θ in (1), which is critical to potential engineering applications — given a desired frequency dependence for the profile of ϵ^* and field localization, values of r and θ can be selected accordingly. This is illustrated in Fig. 5 which displays the θ-dependence of the eigenvalue density $\rho(\lambda,\theta)$ in (a), the spectral function $\mu(\lambda,\theta)$ in (b), the magnitude and phase of the relative effective permittivity ϵ^*/ϵ_2 in (c) and (d) and the IPR in (e), with $r=\sqrt{5}/2$ fixed. Short period systems are indicated by dark horizontal streaks due to associated isolated resonances in μ, with localized regions of yellow. Figure 5a shows that some of these resonances in $\mu(\lambda,\theta)$ are due to resonances in $\rho(\lambda,\theta)$. However, in Figure 5b, the significance of the measure mass becomes apparent, which can diminish eigenvalue resonances or even create resonances in $\mu(\lambda,\theta)$ in regions of low eigenvalue density — also illustrated in the leftmost panel of Figure 3b by the individual eigenvalue $\lambda_j\approx0.32$ with relatively large spectral mass $m_j\gtrsim0.1$. The influence of μ on ϵ^*/ϵ_2 is striking with resonances and features in $|\epsilon^*/\epsilon_2|$ following those in μ, and with an antisymmetry in phase(ϵ^*/ϵ_2) about $\mathrm{Re}\, s\approx0.5$. The IPR values displayed in Fig. 5e again illustrate that resonances in μ are associated either with extremely extended eigenvectors or mobility edges, with large variability in IPR values for a small change in λ. The symmetry $\rho(\lambda)=\rho(1-\lambda)$ well known for the percolation model[26,41] is evident in Fig. 5a for quasiperiodic geometry, and also has symmetry for θ between $\pi/8$ and $3\pi/16$ reminiscent of, but distinctly different from, the Hofstadter-like spectral butterflies observed in the spectra for twisted bilayers and Bloch electrons in magnetic fields[21]. The distinct anomaly in the other figure panels associated with this "butterfly" is due to a region of parameter space associated with very short system period. A careful comparison of the visual features between the eigenvalue density and eigenvector IPR strongly suggests significant correlations between the eigenvalues and eigenvectors.

The eigenvector expansion of $\chi_1\mathbf{E}$ in Eq. (6) provides a clear connection between resonant frequencies and large field intensity when $\mathrm{Im}\, s(\omega)\ll1$. However, our analysis of Fig. 3 also indicates these resonant frequencies correspond to fields that are either extended throughout the medium, as in the leftmost panel of Fig. 3a, or to a mixture of localized and extended states giving rise to more spatially varied field characteristics in both the intensity and localization, as in the leftmost panel of Fig. 2b, with sensitive dependence on frequency.

We now make this correspondence more precise in an analysis of the magnitude and phase of ϵ^* and the localization of $\mathbf{E}$ and $\mathbf{D}$. They are displayed in Fig. 4 for various values of the Moiré twist angle θ, for $0°\le\phi\le2°$, as a function of $\mathrm{Re}\, s(\omega)$. The Drude peak at $\omega=0$ ($s(0)=0$) present for all values of ϕ indicates the composite is conducting for $\omega=0$[39]. For $\phi=0$, at the resonant frequencies both μ and $|\epsilon^*|$ are sharply peaked and ϵ^* diverges as $\mathrm{Im}\, s\to0$. These frequencies correspond to the so-called surface plasmon resonance, which characteristically shows up as a strong absorption line in experiments[39]. At these resonant frequencies ϵ^* also undergoes a dramatic switch in phase which gives rise to an "optical transition," where the material response changes from inductive (metallic) to capacitive (dielectric) — a phenomenon observed in optical cermets[40]. These phase switches also occur at the troughs of $|\epsilon^*|$, where $|\epsilon^*|$ and the mass of μ are small. At these band gap frequencies the material behaves effectively like an electrical insulator. As ϕ increases, the transition frequencies still correspond to the peaks and troughs in $|\epsilon^*|$, though the frequency dependence of these features becomes more irregular.

The IPR for $|\chi_1\mathbf{E}|$ (normalized to unit length) provides a measurement of localization for the electric field itself – equivalently for the normalized displacement field $\chi_1\mathbf{D}=\epsilon_1\chi_1\mathbf{E}$.

Figures 3c and 4b show there is a close relationship between the eigenvector IPR, IPR(**v**), plotted versus λ_j and the electric field IPR, IPR(**E**), plotted versus $\mathrm{Re}\, s(\omega)$, as anticipated above. Specifically, there are frequency regions where the eigenmodes and the electric field are simultaneously localized or extended. Moreover, for $\phi = 0$, 1/8, and 1/2 there are several clear mobility edges in IPR(**E**), following those in IPR(**v**), showing high variability in field localization for small changes in $s(\omega)$, which also correspond to resonant frequencies and high variability in field intensity.

Physical implications. In Figure 2b the localized (loc) and extended (ext) fields for $\phi = 1/8$, 1/2, and 2 were computed for values of $\mathrm{Re}\, s(\omega)$ with optical frequencies ω — indicated by red dots in Figure 4. Comparing these two figures for the panels with values $\phi = 1/8$ and 1/2 further demonstrates the frequency-dependent localization/delocalization transition in the displacement field for the same microstructure. Moreover, the panels for localized (loc) fields in Figure 2b also correspond to resonant peaks in μ in Fig. 3b, which accounts for the high variability in the field intensity in Figure 2b and the amplitude of ϵ^* in Fig. 4a. Furthermore, Fig. 4 for $\phi = 1/8$ and 1/2, shows that toward the infrared end of the spectrum the displacement field is extended and the response of ϵ^* is inductive (metallic), while toward the ultraviolet end of the spectrum the displacement field is more localized and the response of ϵ^* is capacitive (dielectric). There are also band gap frequencies in the optical range.

As ϕ surpasses 1/8, band gap frequencies are absent. The larger checkerboard scale for $|\chi_1 \mathbf{E}|$ shown in Fig. 2b decreases in size and all the material characteristics described above begin to qualitatively resemble those of the random percolation model for $p = p_c$ as $\phi \to 2$. The more regularly distributed eigenvector localization gives rise to spatially varied, meandering, tenuously connected field paths as shown in the corresponding panels of Fig. 3a.

These observations indicate a high degree of tunability in the frequency dependence of the phase and magnitude of ϵ^* and the localization and intensity of **E** and **D**. The resonant and band gap frequencies present for small ϕ are tunable through the microstructure itself via the scale r and Moiré twist angle θ in Eq. (1). We predict that these material characteristics can be reproduced experimentally and tuned by fabrication methods used for etched metallic substrates. (In ref. [46], a small change in Moiré twist angle for bilayer graphene induces a change in conductivity similar to what we observe here for ϵ^*). Since the transformation in Eq. (1) is deterministic, one can also obtain material characteristics similar to those of random systems in a predictable, reproducible manner. This tunability makes our Moiré-type composite class an ideal test bed for potential engineering applications.

Random matrix theory analysis. Statistical quantities for the eigenvalues λ_j of μ provide insights into why the high-density resonances of μ, present for the short period system with $\phi = 0$, spread out as ϕ increases and the system becomes quasiperiodic. The nearest neighbor eigenvalue spacing distribution (ESD) $P(z)$ was initially introduced in random matrix theory to describe fluctuations of characteristic quantities for random systems, but has since accurately described quantities for non-random systems with sufficient complexity[47]. The ESD probes short-range correlations of eigenvalues[47]. For highly correlated Wigner-Dyson (WD) spectra exhibited by, for example, the Gaussian orthogonal ensemble (GOE) of real-symmetric random matrices, the ESD is accurately approximated by $P(z) \approx (\pi z/2)\exp(-\pi z^2/2)$, Wigner's surmise, which illustrates eigenvalue repulsion, vanishing linearly as spacings $z \to 0$[47,48]. In contrast, the ESD for uncorrelated Poisson spectra, $P(z) = \exp(-z)$, allows for significant level degeneracy[47].

Figure 6 a displays the ESD for the eigenvalues λ_j of G for several values of $0° \le \phi \le 2°$. The blue dash-dot curve is the ESD for Poisson spectra, while the green dashed curve is the ESD for the GOE. For $\phi = 0$, 1/64, and 1/32, the sharply peaked resonances in μ with high eigenvalue density give rise to a significant probability of zero spacings, with $P(0) \gtrsim 0.4$. However, as ϕ increases and the composite microgeometry becomes quasiperiodic, the behavior of the ESDs starts to be characterized by weakly correlated Poisson-like statistics[48], also observed for eigenvalues of G for the low volume fraction percolation model[27]. They increase linearly from zero but the initial slope of $P(z)$ is steeper than in the WD case, implying less level repulsion. As $\phi \to 2$, the slope of $P(z)$ decreases, indicating an increase in level repulsion, causing the eigenvalues of μ to spread out as the ESD transitions toward obeying that of the GOE, characterized by highly correlated eigenvalues with strong level repulsion.

A broader overview of the Moiré parameter space. We conclude this section with a discussion of Fig. 6b, which displays the average eigenvector IPR with yellow hues corresponding to short period systems with highly extended eigenmodes — hence displacement fields — and mobility edges, and dark green to blue hues corresponding to quasiperiodic, random-like systems with more regularly distributed eigenmodes and meandering, tenuously connected field paths. Our results here are only a snapshot, which nevertheless reveals the great diversity of this class of composite materials with myriad microgeometric variations, each with a potentially distinct frequency dependence in both the phase and magnitude of ϵ^* and the localization and intensity of **E** and **D**. Figure 1 shows that the arrangement of finite period systems is fractal in nature. It is clear from Figs. 1 and 6b that we have merely scratched the surface in describing this fascinating class of composite materials with tuneable capabilities in both frequency and geometry, potentially enabling materials to be fabricated that achieve desired field characteristics and dielectric responses suitable for a broad range of engineering applications.

Conclusion

A class of Moiré-structured 2D composite materials is introduced. Bulk transport is explored using a Stieltjes integral representation for the effective transport coefficients, and the complex permittivity ϵ^* in particular. The representation involves a spectral measure μ of a real-symmetric matrix G, and a summation formula for the displacement field **D**, involving the eigenvalues λ_i and eigenvectors $\mathbf{v}_i$ of G. The localization properties of **D** and the dielectric profile for ϵ^* are analyzed as the Moiré twist angle θ varies 2 degrees. This small change in θ gives rise to a sharp transition in the microgeometry of the composite material, from periodic to quasiperiodic as the period increases ad infinitum. Short period systems are characterized by sharp resonances in μ which give rise to optical frequencies ω where ϵ^* is sharply peaked (so-called surface plasmon resonance frequencies) and ϵ^* undergoes an "optical transition" from inductive (metallic) to capacitive (dielectric). Band gap optical frequencies are also observed. Moreover, **D** is highly extended for certain ranges of frequency, separated by small "mobility edge" frequency regions of large localization variability, that follow the resonant peaks of μ with high intensity regions of **D**. These characteristics make the dielectric profile and field response highly tunable, a desired feature in engineering applications. As the system is tuned to quasiperiodicity, an increase in eigenvalue repulsion, as measured by the eigenvalue spacing distribution (ESD), causes the sharp

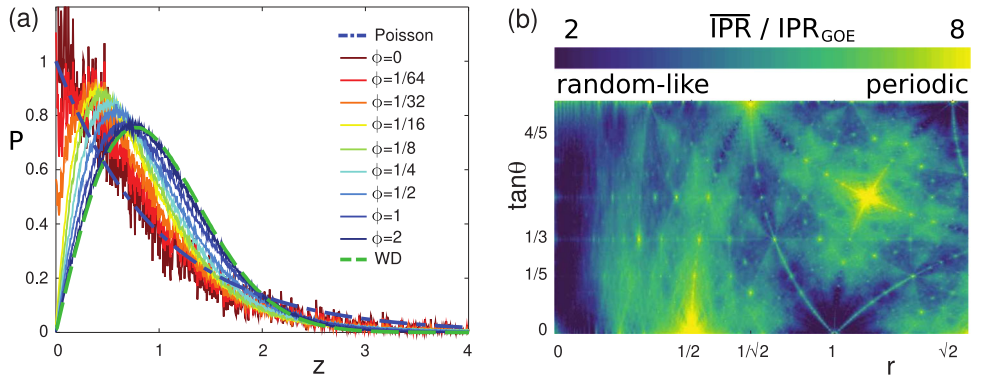

Fig. 6 Eigenvalue spacings and eigenvector localization. (**a**) The eigenvalue spacing distribution (ESD) $P(z)$ for various values of (Moiré) twist angle θ, for $0° \le \phi \le 2°$. The short period system for $\phi = 0$ and those with small twist angles $0 \le \phi \le 1/32$ are characterized by spectral measures μ with very sharp resonances leading to $P(0) \gtrsim 0.4$. However, for $\phi \ge 1/16$ the system begins to transition towards obeying Wigner-Dyson statistics with level repulsion, so that $P(0) = 0$. Level repulsion increases with increasing ϕ as the ESD approaches the Wigner-Dyson ESD, characterized by strong correlations and strong eigenvalue repulsion. (**b**) The ratio of average eigenvector $\overline{IPR}$ with $\mathrm{IPR}_{\mathrm{GOE}} = 3/N_1$ is plotted versus $(r, \tan\theta)$. Yellow hues correspond to short period systems similar to the leftmost panel in Figure 2, characterized by highly extended eigenmodes (hence extended electric and displacement fields) and "mobility edges" with large localization variability. Dark green to blue hues correspond to quasiperiodic systems similar to the one shown in Fig. 2 for $\phi = 2$ with material properties that resemble that of random systems with regularly distributed IPR values and tenuously connected electric and displacement field paths. This panel indicates periodic systems have a repeating pattern that turns out to be fractal in nature, as indicated in Fig. 1. Moreover, quite small changes in the Moiré parameters $(r, \tan\theta)$ result in transitions from ordered periodic systems to disordered quasiperiodic, random-like systems.

resonances of μ to spread out, while the localization characteristics of **D** and the dielectric profile of ϵ^* begin to qualitatively resemble those of the percolation model near its transition point. It is suggested that these material characteristics could be reproduced experimentally and tuned by fabrication methods used for etched metallic substrates.

Code availability

Mathematical and numerical methods used to compute the spectral measures and associated spectral statistics displayed in this manuscript are detailed in ref. [26]. Associated code will be made available upon reasonable request.

Data availability

Numerical data used to generate figures in this manuscript will be made available upon reasonable request.

Received: 27 July 2021; Accepted: 26 April 2022;
Published online: 14 June 2022

References

1. Yablonovitch, E. Inhibited spontaneous emission in solid-state physics and electronics. *Phys. Rev. Lett.* **58**, 2059–2062 (1987).
2. Yablonovitch, E. & Gmitter, T. J. Photonic band structure: the face-centered-cubic case. *Phys. Rev. Lett.* **63**, 1950–1953 (1989).
3. John, S. Strong localization of photons in certain disordered dielectric superlattices. *Phys. Rev. Lett.* **58**, 2486–2489 (1987).
4. Joannopoulos, J. D., Johnson, S. G., Winn, J. N. & Meade, R. D. *Photonic Crystals: Molding the Flow of Light, Second Edition* (Princeton University Press, 2008).
5. Shechtman, D., Blech, I., Gratias, D. & Cahn, J. W. Metallic phase with long-range orientational order and no translational symmetry. *Phys. Rev. Lett.* **53**, 1951–1953 (1984).
6. Levine, D. & Steinhardt, P. J. Quasicrystals: a new class of ordered structures. *Phys. Rev. Lett.* **53**, 2477–2480 (1984).
7. Dubois, J.-M. Properties and applications of quasicrystals and complex metallic alloys. *Chem. Soc. Rev.* **41**, 6760–6777 (2012).
8. Vardeny, Z. V., Nahata, A. & Agrawal, A. Optics of photonic quasicrystals. *Nat. Photon.* **7**, 177–187 (2013).
9. Kohmoto, M., Sutherland, B. & Iguchi, K. Localization of optics: quasiperiodic media. *Phys. Rev. Lett.* **58**, 2436–2438 (1987).
10. Edagawa, K. Photonic crystals, amorphous materials, and quasicrystals. *Sci. Technol. Adv. Mater.* **15**, 034805 (2014).
11. Rechtsman, M. C., Jeong, H.-C., Chaikin, P. M., Torquato, S. & Steinhardt, P. J. Optimized structures for photonic quasicrystals. *Phys. Rev. Lett.* **101**, 073902 (2008).
12. Peach, M. Quasicrystals step out of the shadows. *Mater. Today* **9**, 44–47 (2006).
13. Kraus, Y. E., Lahini, Y., Ringel, Z., Verbin, M. & Zilberberg, O. Topological states and adiabatic pumping in quasicrystals. *Phys. Rev. Lett.* **109**, 106402 (2012).
14. Verbin, M., Zilberberg, O., Kraus, Y. E., Lahini, Y. & Silberberg, Y. Observation of topological phase transitions in photonic quasicrystals. *Phys. Rev. Lett.* **110**, 076403 (2013).
15. Verbin, M., Zilberberg, O., Lahini, Y., Kraus, Y. E. & Silberberg, Y. Topological pumping over a photonic Fibonacci quasicrystal. *Phys. Rev. B* **91**, 064201 (2015).
16. Kollár, A., Fitzpatrick, M. & Houck, A. Hyperbolic lattices in circuit quantum electrodynamics. *Nature* **571**, 45–50 (2019).
17. Yang, Z., Lustig, E., Lumer, Y. & Segev, M. Photonic Floquet topological insulators in a fractal lattice. *Light Sci. Appl.* **9**, 32704361 (2020).
18. Carr, S. et al. Twistronics: manipulating the electronic properties of two-dimensional layered structures through their twist angle. *Phys. Rev. B* **95**, 075420 (2017).
19. Bellissard, J. & Simon, B. Cantor spectrum for the almost Mathieu equation. *J. Funct. Anal.* **48**, 408–419 (1982).
20. Etter, S., Massatt, D., Luskin, M. & Ortner, C. Modeling and computation of Kubo conductivity for two-dimensional incommensurate bilayers. *Multiscale Model. Simul.* **18**, 1525–1564 (2020).
21. Rosa, M. I. N., Ruzzene, M. & Prodan, E. Topological gaps by twisting. *Commun. Phys.* **4**, 130 (2021).
22. Bergman, D. J. Exactly solvable microscopic geometries and rigorous bounds for the complex dielectric constant of a two-component composite material. *Phys. Rev. Lett.* **44**, 1285–1287 (1980).
23. Milton, G. W. Bounds on the complex dielectric constant of a composite material. *Appl. Phys. Lett.* **37**, 300–302 (1980).
24. Golden, K. & Papanicolaou, G. Bounds for effective parameters of heterogeneous media by analytic continuation. *Commun. Math. Phys.* **90**, 473–491 (1983).
25. Milton, G. W. *The Theory of Composites*. Cambridge Monographs on Applied and Computational Mathematics (Cambridge University Press, 2002).
26. Murphy, N. B., Cherkaev, E., Hohenegger, C. & Golden, K. M. Spectral measure computations for composite materials. *Commun. Math. Sci.* **13**, 825–862 (2015).
27. Murphy, N. B., Cherkaev, E. & Golden, K. M. Anderson transition for classical transport in composite materials. *Phys. Rev. Lett.* **118**, 036401 (2017).
28. Golden, K., Goldstein, S. & Lebowitz, J. L. Classical transport in modulated structures. *Phys. Rev. Lett.* **55**, 2629–2632 (1985).
29. Golden, K., Goldstein, S. & Lebowitz, J. L. Discontinuous behavior of effective transport coefficients in quasiperiodic media. *J. Stat. Phys.* **58**, 669–684 (1990).

30. Simon, B. Almost periodic Schrödinger operators: a review. *Adv. Appl. Math.* **3**, 463–490 (1982).
31. Ostlund, S., Prandit, R., Rand, D., Schnellnhuber, H. J. & Siggia, E. D. One dimensional Schrödinger equation with an almost periodic potential. *Phys. Rev. Lett.* **50**, 1873–1877 (1983).
32. Kohmoto, M. & Oono, Y. Cantor spectrum for an almost periodic Schrödinger equation and a dynamical map. *Phys. Lett. A* **102**, 145–148 (1984).
33. Arakelian, S. et al. Formation of quasiperiodic bimetal thin films with controlled optical and electrical properties. In Andrews, D. L., Nunzi, J.-M. & Ostendorf, A. (eds.) *Nanophotonics VI*, vol. 9884, 509-516. International Society for Optics and Photonics (SPIE, 2016).
34. Nandhagopal, P., Pal, A. K. & Bharathi Mohan, D. Fabrication of silver and silver-copper bimetal thin films using co-sputtering for SERS applications. *Opt. Mater.* **97**, 109381 (2019).
35. Genov, D. A., Sarychev, A. K., Shalaev, V. M. & Wei, A. Resonant field enhancements from metal nanoparticle arrays. *Nano Lett.* **4**, 153–158 (2004).
36. Genov, D. A., Shalaev, V. M. & Sarychev, A. K. Surface plasmon excitation and correlation-induced localization-delocalization transition in semicontinuous metal films. *Phys. Rev. B* **72**, 113102 (2005).
37. Dallapiccola, R., Gopinath, A., Stellacci, F. & Negro, L. D. Quasi-periodic distribution of plasmon modes in two-dimensional Fibonacci arrays of metal nanoparticles. *Opt. Express* **16**, 5544–5555 (2008).
38. Shenhar, R. & Rotello, V. Nanoparticles: scaffolds and building blocks. *Acc. Chem. Res.* **36**, 549–561 (2003).
39. Bergman, D. J. & Stroud, D. Physical properties of macroscopically inhomogeneous media. *Phys. Solid State* **46**, 147–269 (1992).
40. Clerc, J. P., Giraud, G., Laugier, J. M. & Luck, J. M. The electrical conductivity of binary disordered systems, percolation clusters, fractals, and related models. *Adv. Phys.* **39**, 191–309 (1990).
41. Jonckheere, T. & Luck, J. M. Dielectric resonances of binary random networks. *J. Phys. A Math. Theor.* **31**, 3687–3717 (1998).
42. Stauffer, D. & Aharony, A. *Introduction to Percolation Theory, Second Edition*. (Taylor and Francis, London, 1992).
43. Torquato, S. *Random Heterogeneous Materials: Microstructure And Macroscopic Properties*. (Springer-Verlag, New York, 2002).
44. Cherkaev, E. Inverse homogenization for evaluation of effective properties of a mixture. *Inverse Probl.* **17**, 1203–1218 (2001).
45. Losurdo, M., Moreno, F., Cobet, C., Modreanu, M. & Pernice, W. Plasmonics: enabling functionalities with novel materials. *J. Appl. Phys.* **129**, 220401 (2021).
46. Zhang, S. et al. Abnormal conductivity in low-angle twisted bilayer graphene. *Sci. Adv.* **6**, eabc5555 (2020).
47. Guhr, T., Müller-Groeling, A. & Weidenmüller, H. A. Random-matrix theories in quantum physics: Common concepts. *Phys. Rep.* **299**, 189–425 (1998).
48. Canali, C. M. Model for a random-matrix description of the energy-level statistics of disordered systems at the Anderson transition. *Phys. Rev. B* **53**, 3713–3730 (1996).

Acknowledgements

We gratefully acknowledge support from the Division of Mathematical Sciences at the U.S. National Science Foundation through Grant DMS-1715680 and the Office of Naval Research Applied and Computational Analysis Program through Grants N00014-18-1-2552 and N00014-21-1-2909. We thank Valy Vardeny and Sarah Li for helpful conversations. We also thank one of the reviewers for suggesting the creation of Fig. 5. Finally, we would like to thank Joel Lebowitz and Shelly Goldstein for originally asking the question about the behavior of classical transport in quasiperiodic media almost four decades ago, which helped lead to the current investigation.

Author contributions

D.M., N.B.M., E.C., and K.M.G. collaborated in developing the ideas in this study and analysing the results. D.M. and N.B.M. performed most of the numeric computations.

Competing interests

All authors declare no competing interests.

Additional information

Supplementary information The online version contains supplementary material available at https://doi.org/10.1038/s42005-022-00898-z.

Correspondence and requests for materials should be addressed to Kenneth M. Golden.

Peer review information *Communications Physics* thanks the anonymous reviewers for their contribution to the peer review of this work. Peer reviewer reports are available

Reprints and permission information is available at http://www.nature.com/reprints

Publisher's note Springer Nature remains neutral with regard to jurisdictional claims in published maps and institutional affiliations.